RSC Advances

PAPER

View Article Online
View Journal | View Issue

Cite this: *RSC Adv.*, 2023, **13**, 31756

Facile fabrication of plasmonic Ag/ZIF-8: an efficient catalyst for investigation of antibacterial, haemolytic and photocatalytic degradation of antibiotics†

Asima Subhadarshini,[a,c] Sangram Keshari Samal,[b] Ananya Pattnaik[b] and Binita Nanda *[c]

Received 19th July 2023
Accepted 10th October 2023

DOI: 10.1039/d3ra04851a

rsc.li/rsc-advances

Present article represents the fabrication of plasmonic Ag/ZIF-8 composite and its effect on antibacterial, haemolytic and photocatalytic degradation of antibiotics. Ag/ZIF-8 was prepared by varying molar concentrations (1 mM, 2.5 mM, and 5 mM) of $AgNO_3$ into ZIF-8 using $NaBH_4$ as a reducing agent by the sol–gel process. The material was then characterised using the XRD, XPS, FTIR, SEM, HRTEM, UVDRS, BET and EIS techniques. When it comes to breaking down the antibiotic CIP, the optimised Ag2.5/ZIF-8 exhibits the strongest photocatalytic capability, with a degradation efficiency of 82.3% after 90 minutes. Due to LSPR (Localised Surface Plasmon Resonance) as well as the efficient movement and separation of the interfaces of photo-generated charge carriers in Ag2.5/ZIF-8 may be the causes of this increase in photocatalytic degradation. The effect of several parameters, such as pH, a variety of catalysts, varying dose concentrations, scavenging and sustainability are being investigated. The para benzoquinone ($OH^•$) and citric acid (h^+) the primary active species in the photocatalytic breakdown pathway, according to trapping study. Whereas, Ag5/ZIF-8 was optimised for greater antibacterial activity against *S. aureus* and *E. coli* due to the synergistic impact of Ag^+ and Zn^{2+} in Ag5/ZIF-8 and in haemolytic experiment, all samples were discovered to be non-toxic to blood cells. Overall, the synthesised compound was discovered to be a reusable, affordable catalyst for water remediation that can also be used in biomedicine.

1. Introduction

The rapid rate of bacterial reproduction has historically had a huge, negative and pervasive impact on human health. Due to their growth and evolution clinical therapy through antibiotics has begun as an early treatment. Besides that, the targeted bacteria might gradually create a compensatory mechanism to counteract the antibiotics inhibitory effects and results in formation of more harmful bacteria with greater resistance. This antibiotic resistance could result in infectious disease that are more dangerous to human health.[1–4] Therefore, many nanoscale materials with exceptional antibacterial properties have been developed and manufactured to combat this drug resistant microorganism.[5,6] Moreover, bacteria can barely form immune system in the nanomaterial antibacterial system due to the special antimicrobial mechanism. In addition to antibiotic resistance bacteria induced environmental issue, the rapid industrialisation has resulted in unchecked release of drugs leading to serious environmental pollution. CIP is a fluoroquinolone antibiotic used to treat no. of bacterial diseases[7–9] which cannot easily be metabolised in animal body and are sometimes released to waterbodies and which has become a threat to environment. All though various techniques are followed for removal of antibiotics in water bodies but Advanced Oxidation Process (AOP) is under demand in current days due to its high efficiency and excellent performance. Among which photocatalysis is a method reported to have energy saving property as it uses abundant solar energy to catalyse chemical reactions also an adaptable and cost-effective water treatment technology.[10–12]

Many research on the breakdown of antibiotics have also been conducted using Metal Organic Framework (MOF) based photocatalysts.[13–15] MOFs are a type of porous material having intra molecular pores formed *via* coordination by generating nodes of metal ions or metal ion clusters and employing numerous organic ligands forming framework support.[16–19] They are employed in a variety of applications, such as gas storage, sensors, adsorption, antibacterial agents and

---

[a] *Environmental Science, Department of Chemistry, Faculty of Engineering and Technology (ITER), Siksha 'O' Anusandhan (Deemed to be) University, Bhubaneswar, Odisha, India 751030*

[b] *Laboratory of Biomaterials and Regenerative Medicines for Advanced Therapies, ICMR-Regional Medical Research Centre, Bhubaneswar, Odisha, India-751023*

[c] *Department of Chemistry, Faculty of Engineering and Technology (ITER), Siksha 'O' Anusandhan (Deemed to be) University, Bhubaneswar, Odisha, India-751 030. E-mail: binitananda@soa.ac.in*

† Electronic supplementary information (ESI) available. See DOI: https://doi.org/10.1039/d3ra04851a

catalysis.[20] MOFs have the following benefits over typical photocatalytic semiconductors. First off, the open frame structure and porosity of MOFs make it easier for damaged materials to diffuse to the catalyst's active sites. Secondly, MOFs have a highly variable porosity and extraordinarily high specific surface area. These characteristics make composite catalytic materials with other active ingredients feasible. Lastly, adding functional groups can effectively control the spectrum response range of MOFs.[21] These considerations have led to the MOF groups increasing significance in photocatalysis, particularly in the area of organic pollutant degradation. Moreover, conventional MOFs have limits when used as photocatalysts, just as conventional photocatalytic materials. Composite catalysts are another popular technique, additionally just employing MOFs as catalysts. The restrictions can be balanced out synergistically and catalytic activity can be maximised by employing certain composite processes (heterojunction structures) and choosing active suitable materials.[15] Among MOFs, zeolitic imidazolate frameworks (ZIFs) are a subclass.[22–24] Its geometry is similar to that of zeolites, which is why they were given that name. ZIF-8 is among this groups most frequently used framework. Showing excellent features include a large specific surface area, adjustable channels and exceptional thermal and chemical stability.[25–27] Nevertheless, the photo-catalytic performance depends upon the wide band gap of ZIF-8. The heterojunction approach, which involves the coupling of semiconductors with narrow band gaps, is a quick and effective way of enhancing photocatalytic efficiency. It can aid in electron transport with the rate of photo-generated electron reduction and hole recombination. The photodegradation method is used to purify organically contaminated wastewaters by silver nanoparticles[28] and their compounds, such as Ag_3VO_4, Ag_2O, Ag_2S, Ag_3PO_4, Ag_2CO_3, but notably silver halides (AgX, $X = I$, Br and Cl), have been widely used up to this point. Additionally, the photocatalyst can be extended to the visible light response range by decorating it with noble metals (Au, Ag, Pt, *etc.*) due to the strong localised surface plasmon resonance (LSPR) effect and *via* a synergistic effect.[29,30] In ZIF-8 structure, the Zn^{2+} cations can boost antibacterial activity of silver ions. According to the aforementioned qualities, reduced Ag/ZIF-8 composite has a lot of potential as a good photocatalyst.

Till now, minimal research of reduced Ag/ZIF-8 photocatalyst on the environmental usage, potential for eliminating drugs, antibacterial activity and haemolytic properties has been reported. In this study, we developed an *in situ* solgel technique to prepare a porous reduced silver-doped ZIF-8 photocatalyst for the elimination of the antibiotic CIP. Additionally, two types of bacteria (Gram Positive and Gram negative) were used to assess the synthesised material's antibacterial capability and haemolytic activity. By using the impregnation approach, different molar variations of silver were loaded into the surface of ZIF-8. The findings of this study suggest that adding reduced silver to the porous ZIF-8 framework's surface and interior enhances the catalysts capacity to catalyse the breakdown of the medication utilised in this study.

2. Synthesis procedure

2.1. Materials

Zinc nitrate hexahydrate (99%, SRL), 2-methylimidazole (99%, SRL), sodium hydroxide pellets (Merck), silver nitrate (99.5%, SRL), sodium boro-hydrate (Extra-pure, SRL) and CIP ($C_{17}H_{18}FN_3O_3$, 98%, Himedia). These chemicals utilised in this work are analytical grade reagents (AR) and that had not been purified further.

2.2. Synthesis of ZIF-8 (nanoparticles)

ZIF-8 was prepared of equal molar ratio concentration (1 : 1) of (2.97 g, 1 mol) of Zn ($NO_3 \cdot 6H_2O$) by dissolving in 10 mL of

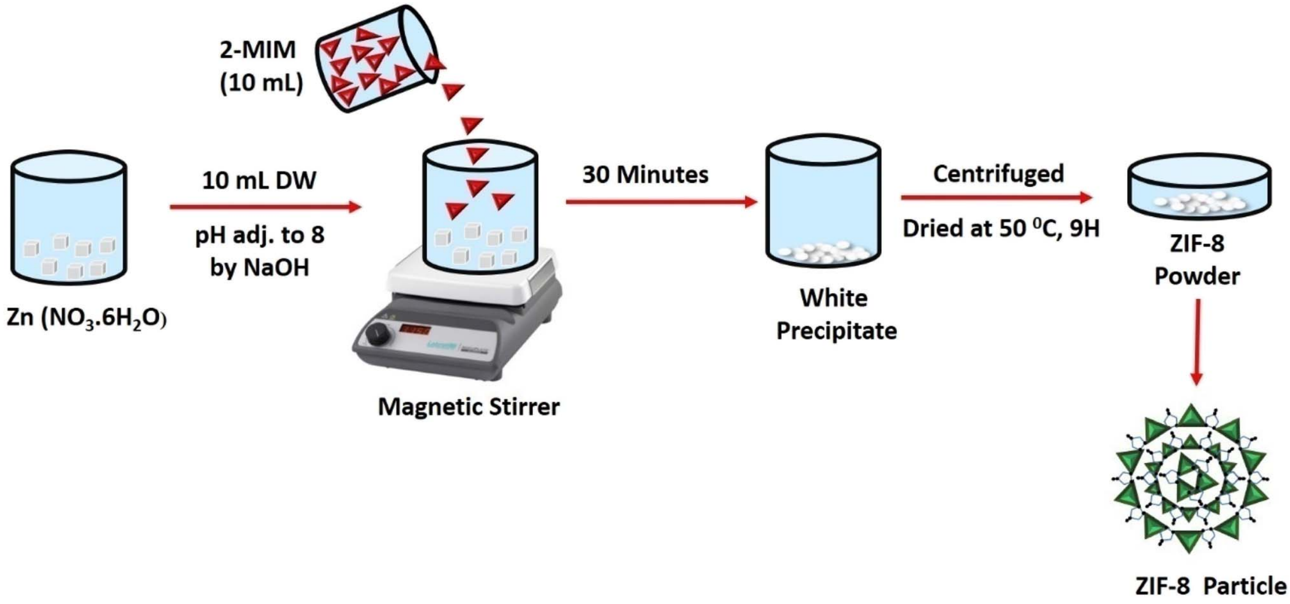

Fig. 1 Diagrammatic representation of ZIF-8 synthesis.

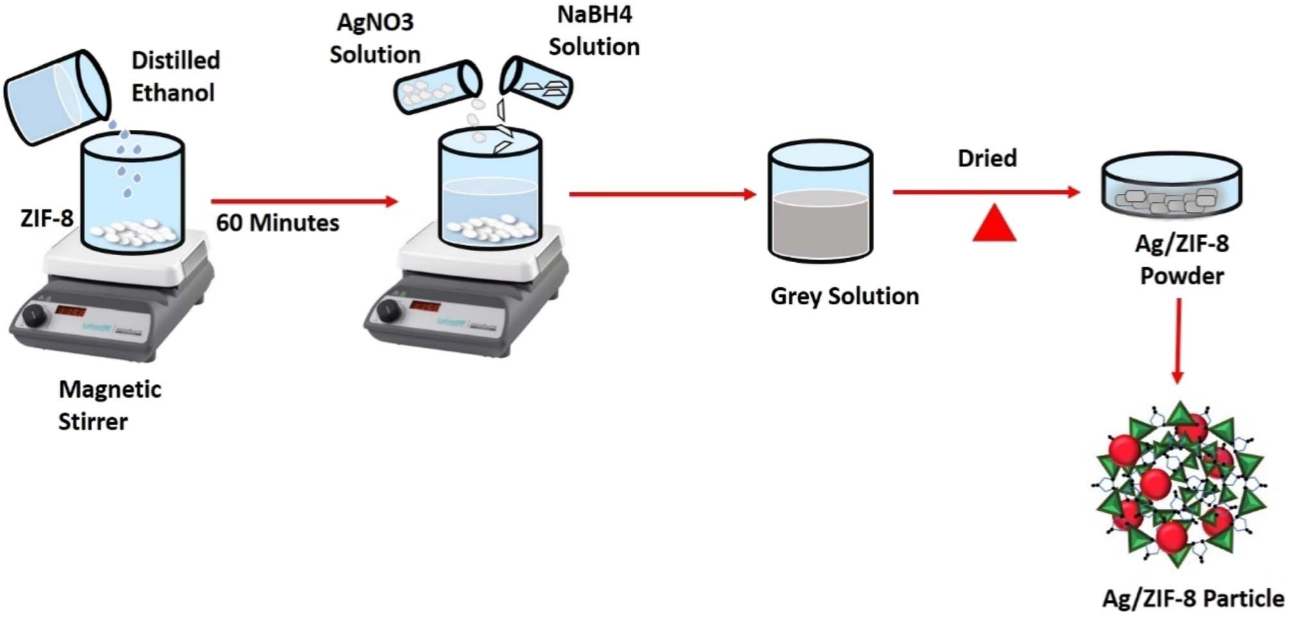

Fig. 2 Schematic diagram of synthesis of Ag/ZIF-8 (reduced).

distilled water (NaOH was used to adjust the pH to 8) and 2-methylimidazole (0.82 g, 1 mol), in 10 mL distilled water (added dropwise). The mixture was then agitated for 30 minutes. A white precipitate obtained and was centrifuged further at (11 000 rpm, 10 minutes) followed by washing four times. The obtained white powder was then dried at 50 °C and named ZIF-8 in Fig. 1.

2.3. Fabrication of reduced Ag decorated ZIF-8

In 500 mL of distilled ethanol, 1 g of ZIF-8 was scattered and continuous stirred for 1 h. Followed then 5 mL of 1 mM $AgNO_3$ solution was added, then 5 mL of 2 mM $NaBH_4$ was added as a reducing agent. Then the fluid gradually changed to ash grey in colour. In similar way 2.5 mM and 5 mM of $AgNO_3$ solution was added and different molar ratio samples were obtained. The solutions were further heated over a hot plate until complete evaporation of the solvent. Then the resultant substance was dried in an oven and named AZ1, AZ2.5 and AZ5 depicted in Fig. 2.

2.4. Characterization of nanoparticles

The broad angle X-ray diffraction study of the materials was measured with a scanning range of 10° to 80° using Rigaku Miniflex diffractometer (at $\lambda = 1.5406$ Å CuKα radiation). A Kratos Axis-165 X-ray photoelectron spectra with a MgK source was used for X-ray photoelectron spectroscopy. Fourier transforms infrared spectra was used to characterise the functional groups by measuring the molecular vibrations of the samples using Jasco FT/IR-4600LE. The materials were compacted into pellets by combined with potassium bromide (KBr) and the IR absorption range 400–4000 cm^{-1} was set to determine. The optical study was measured through UV-DRS spectra with boric acid used as a reference, by using Jasco-750 UV-Vis Spectrophotometer within 200–800 nm range. The surface morphologies were studied using a JEOL SEM Model JSM-6390 for scanning electron microscope and JEOL JEM 2100 PLUS for transmission electron microscope. The Brunauer–Emmett–Teller techniques (Quanta chrome Auto sorb) was used to determine pore volume, pore diameter and surface area of the samples.

2.5. Experiments

2.5.1. MIC (minimum inhibitory concentration). Antibacterial activity and efficiency against *S. aureus* (ATCC 25923) (Gram-positive) and *E. coli* (ATCC 25922) (Gram-negative) of synthesized samples were evaluated through the measurements of the minimal concentration which inhibits the growth of the strains. For the determination of MIC broth microdilution method was used and 96 well-plate method was followed. To the plate 264 μL of MHB (Mueller Hinton Broth) was added to 1st column and then 150 μL added from 2nd column to 12th column. 10 μL of the bacterial fresh culture suspension which was already taken for incubation overnight was added to each column except negative control (NC); it contains only nutrient broth and the positive control (PC); it contains both nutrient broth and bacterial culture. Then 36 μL of the 4 Samples (ZIF-8, AZ1, AZ2.5, AZ5 variations) were added to the first column to make the volume 300 μL. After mixing properly from the 1st column 150 μL was transferred to the 2nd column likewise serial dilution was followed up to the 10th column and finally from the 10th column 150 μL of solution was discarded. The plate was then kept overnight and optical density (OD) was recorded using Thermo-scientific Elisa Reader at wavelength 600 nm.

2.5.2. Antibacterial activity. The antibacterial properties for ZIF-8, AZ1, AZ2.5 and AZ5 samples were investigated by using Agar well diffusion method. Fresh culture of Gram-positive *S.*

aureus (ATCC 25923) and Gram-negative *E. coli* (ATCC 25922) were used. First, 20 mL of MHB agar medium was put in a sterilised Petri plate then allowed to solidify at room temperature followed with the corresponding strains of bacteria. Then a 6 mm diameter well was created with a sterile cork borer. Then, 60 μL of each sample was deposited in the well at a concentration of 10 mg mL^{-1} and the plates were incubated for 24 hours at 37 °C. The diameter of the inhibitory growth was then measured using a millimetre scale.

2.5.3. Haemolytic activity. Blood plate assay method was used for the haemolysis test. Initially fresh human blood (2.5 mL) was taken from a healthy human donor and mixed into 50 mL of blood agar base, allowed for autoclave and were then poured into sterilized Petri plates further keeping it to solidify. Then 10 μL of ZIF-8, and AZ1, AZ2.5 and AZ5 at a concentration of 10 mg mL^{-1} were tested, 1% of SDS solution and DMSO were poured on to the blood agar plate and incubated at 37 °C overnight. 1% of SDS (Sodium Dodecyl Sulphate) solution was used as a positive control, and DMSO (Dimethyl Sulfoxide) was used as a negative control.

2.5.4. Processing of bacterial sample for scanning electron microscope (SEM). The morphology of bacteria was observed by SEM after antibacterial treatments. The obtained bacterial suspensions (*E. coli* and *S. aureus*) were washed with PBS buffer for three times at 6000 rpm for 2 minutes. Followed the bacterial cells were fixed with 2.5%, glutaraldehyde at 4 °C overnight and the alcohol dehydration was done by using an ethanol aqueous solution at ethanol concentrations 30%, 50%, 70%, 80%,90% and 100% for 10 minutes each. Then sample were dried by the vacuum freeze-drying method. The dried samples were then coated with gold by sputtering and observed by SEM (Hitachi HUS-5Gb).

2.5.5. Investigation of photocatalytic degradation

2.5.5.1. Photo-oxidation of CIP. Under sunlight, photocatalytic applications against the degradation of the antibiotic drug CIP were investigated using the synthesised catalysts pristine ZIF-8, AZ1, AZ2.5 and AZ5. To maintain the adsorption–desorption equilibrium, 0.02 g of photocatalyst was dispersed in 40 ppm of 20 mL of CIP solution and agitated for 15 minutes in the dark. The photo-oxidation of CIP solution was examined by subjecting it to the sun at an illumination level of 100 000 lux for 90 minutes in Bhubaneswar, Odisha, between 12 p.m. to 2 p.m. The photocatalyst was recovered by filtration after degradation and the filtrate was examined through a UV-visible spectrophotometer (SYSTRONICS-2022) at 275 nm. The photo-oxidation efficacy of the photocatalyst on CIP was calculated using the following equation:

$$\text{Efficiency}(\%) = \frac{(C_0 - C_t)}{C_0} \times 100.$$

where C_0 is the starting pollutant concentration and C_t is the last recorded pollutant concentration after the reaction.

2.5.5.2. Photoelectrochemical experiment. Electrochemical impedance spectra (EIS) were studied by the electrical behaviour of ZIF-8, AZ1, AZ2.5 and AZ5 was investigated using an LCR metre of type No-N4L PSM, 1735 throughout a wide frequency range (1 kHz to 1 MHz). The Nyquist plot analysis offers precise information regarding grain, grain boundaries, electrode polarisation and the effect of electron–hole separation in these samples. The Nyquist plot may also show how grain and grain borders affect the electrical conduction process. With the aid of the ZSIMPWIN version 2.0 software Nyquist plot were fitted.

3. Results and discussion

3.1. Crystallographic study

Fig. 3 shows the structural properties of ZIF-8 and composites (AZ1, AZ2.5 and AZ5) examined using a Rigaku X-ray diffractometer with CuKα over a large range of Bragg's angle 2θ ($10° \le 2\theta \le 80°$). The distinct and significant peak at 2θ angle values 10.40°, 12.73°, 14.69°, 16.45°, 18.03°, 22.12°, 24.49°, 26.65°, 29.9°, 30.85°, 31.76° and 32.51° exhibits a high crystallinity sodalite (SOD) type structure related to the diffraction (*hkl*) planes at (002), (112), (022), (013), (222), (114), (233), (134), (044), (334), (244) and (235) respectively according to the other samples that were reported having (JCPDS no. 00-062-1030) of ZIF-8.[31] The presence of peaks in diffraction at 2θ angles 38.1° and 64.4° corresponds to typical face centred cubic structure diffraction peaks of silver at (111) and (220) diffraction (*hkl*) planes respectively having (JCPDS no. 01-087-0719).These peaks were more pronounced, suggesting that silver ions had been effectively incorporated into the ZIF-8's porous surface and structure, indicating the as synthesised composite was of high purity and the diffraction pattern at 30° and 28.9° shows the presence of addition of $NaBH_4$ to the previously synthesized composite forming Ag/ZIF-8 (reduced).[32,33]

3.2. Chemical composition study

Using XPS, the surface composition, electrical environment and chemical environment of ZIF-8 and AZ2.5 were investigated as shown in Fig. 4. Through the distinctive survey scan peaks, the presence of various elements such as silver, carbon, nitrogen, zinc and oxygen were confirmed. The survey XPS spectra of the

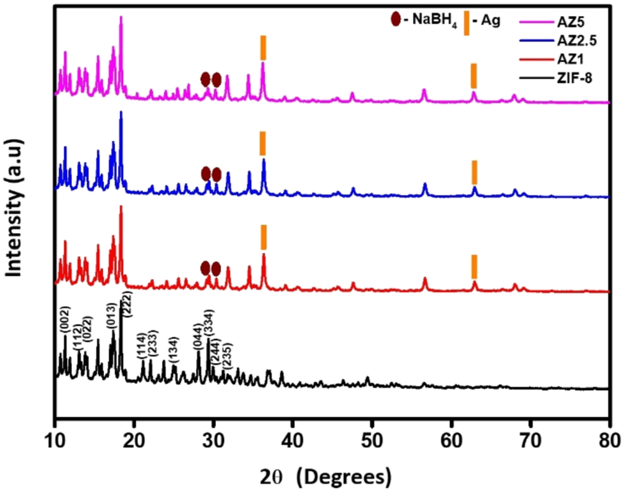

Fig. 3 Powdered X-ray Diffraction Pattern of pristine ZIF-8, AZ1, AZ2.5 and AZ5.

different electronic states of Zn2p, N1s, C1s, O1s, and Ag3d was displayed in Fig. 4(a). The existence of divalent Zn^{2+} in both ZIF-8 and Ag/ZIF-8 was proved through the two typical peaks of $Zn2p^{1/2}$ and $Zn2p^{3/2}$ are at 1045.01 and 1022.19 eV respectively are given in Fig. 4(b). Fig. 4(c) shows the fine spectrum of C1s, which divided into two peaks by the peak splitting software and

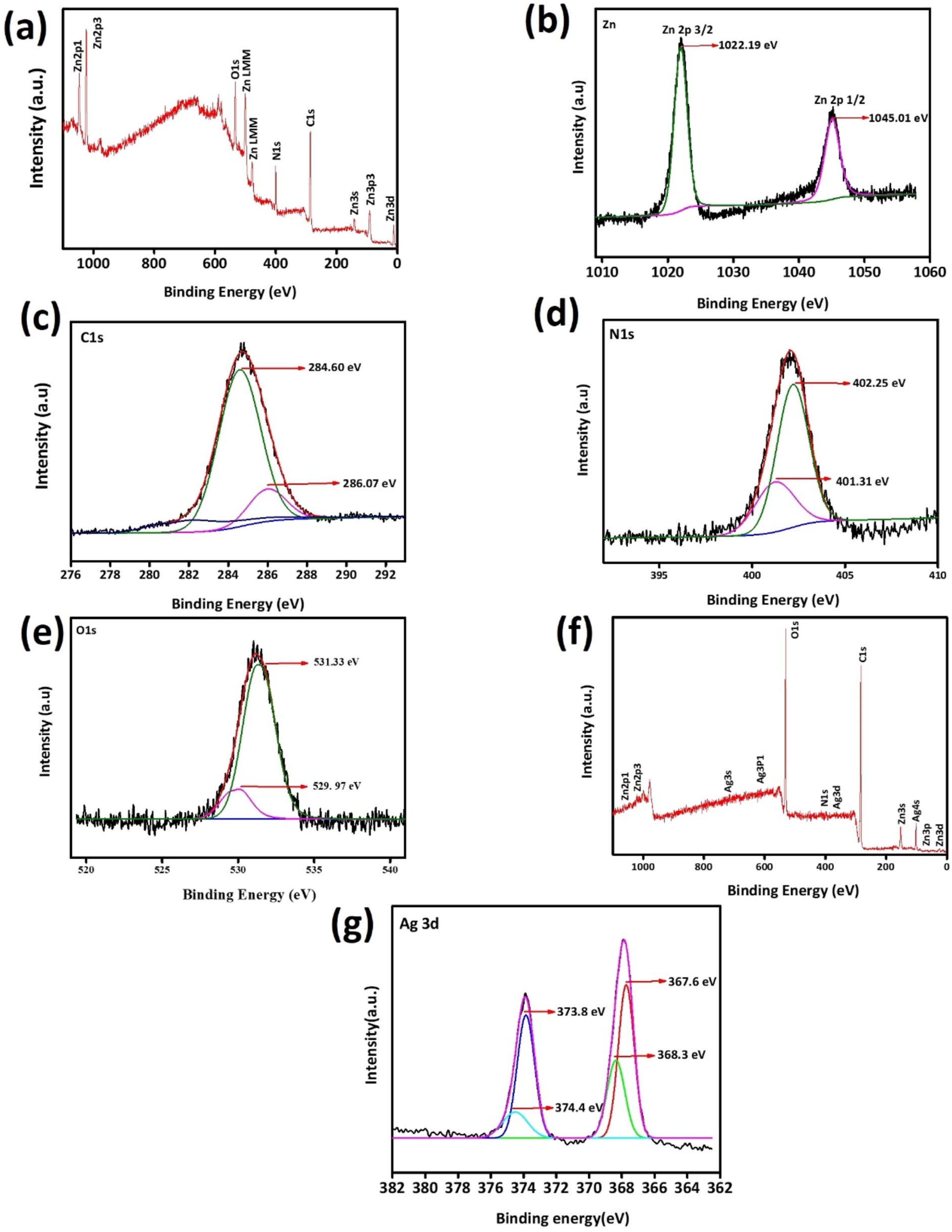

Fig. 4 X-ray photoelectron spectroscopy of ZIF-8 and AZ2.5 Material: (a) XPS survey curve of ZIF-8, (b) high resolution spectrum of Zn2p, (c) C1s, (d) N1s, (e) O1s, (f) XPS survey spectra of AZ 2.5 and (g) resolution spectrum of Ag3d.

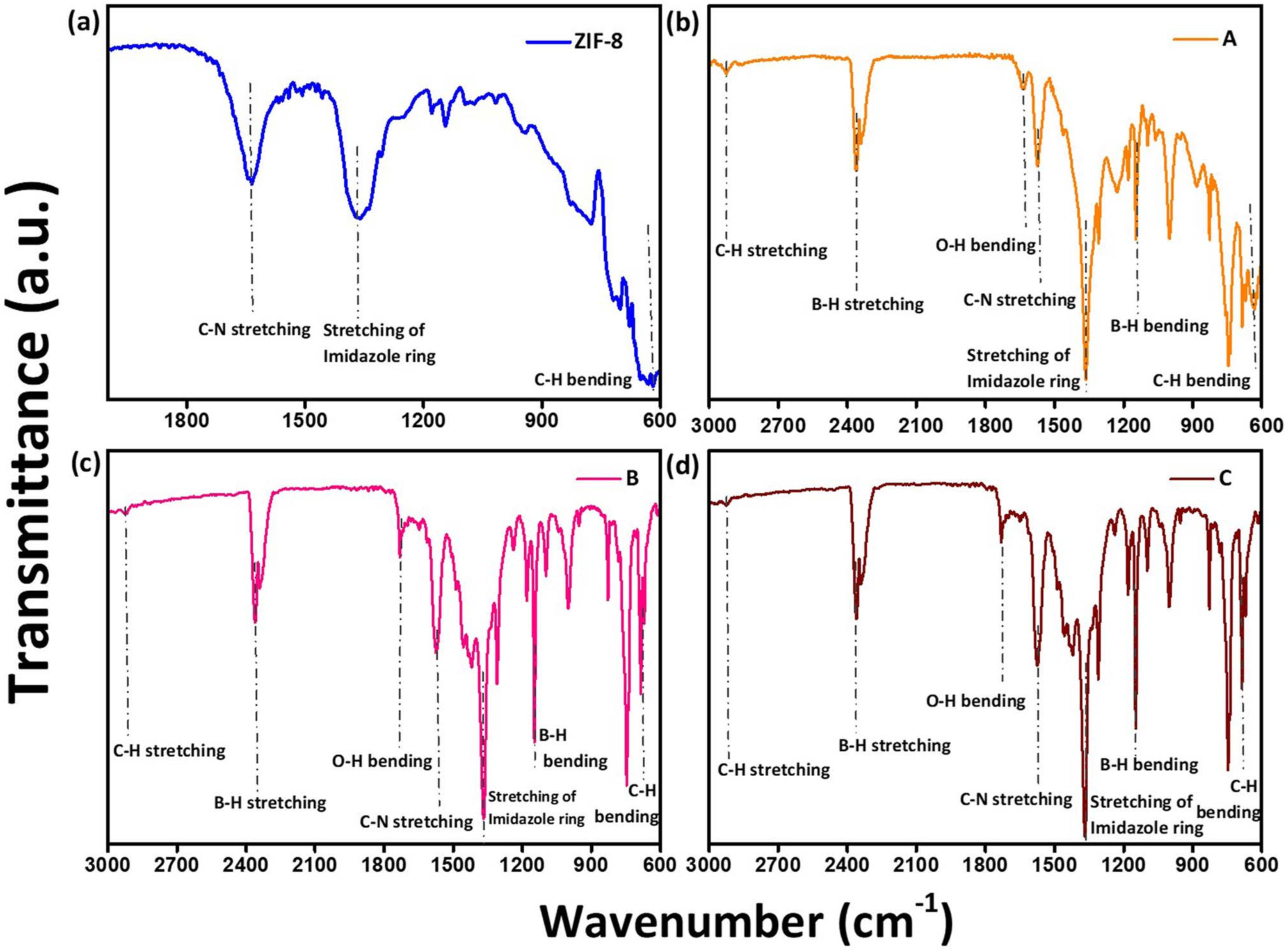

Fig. 5 FTIR spectroscopy of (a) ZIF-8, (b) AZ1, (c) AZ2.5 and (d) AZ5.

appeared at 284.60 eV because of the presence of C–C bond on the size chain of imidazole. The extra peaks showed 286.07 eV depicting C–N bonds on the imidazole ring. XPS spectrum of N1s is shown in Fig. 4(d) having peaks at 401.31 eV and 402.25 eV correspond to C═N–Zn and N═C respectively. In Fig. 4(e) the O1s peak can be resolved into 2 peaks with a binding energy centred at 531.33 eV and 529.97 eV. The peak value of 529.97 eV corresponds to the hypoxic (oxygen vacancy) sites or oxygen ions (chemically adsorbed oxygen) on the surface of the material. The peak value of 531.33 eV corresponds to the lattice oxygen (O^{2-}) in Ag/ZIF-8 and ZIF-8.[34] Fig. 4(f) provides the survey scan of Ag/ZIF-8 to investigate the presence of Ag in (Ag^0 or Ag^+) the as synthesized composite. As can be seen in Fig. 4(g), Ag $3d^{5/2}$ and Ag $3d^{3/2}$ signals reveals that the binding energy corresponds to 368.09 eV and 374.11 eV, respectively, which shows the presence of metallic Ag(0). The findings imply that the composite contains Ag in a metallic form. The XPS data unequivocally demonstrate that the structure of ZIF-8 contains an Ag atom that has been thoroughly doped.[35]

3.3. Functional study

Fig. 5(a)–(d) shows the presence of distinct functional groups in ZIF-8, AZ1, AZ2.5 and AZ5 composites at wavelengths ranging from 600 to 2000 cm^{-1} for ZIF-8 and 600 to 3000 cm^{-1} for Ag modified ZIF-8 composites. The band at 1584 cm^{-1} corresponds to the stretching mode of C–N bonding in HMIM. The wave numbers ranging from 600 to 1500 cm^{-1} indicate the bending and stretching forms of the imidazole rings. The stretching vibration of the imidazole ring is revealed by the distinctive peak at 1423 cm^{-1}. Furthermore, the peak at 694.3 cm^{-1} is due to aromatic sp^2 C–H bending.[32] Additionally, the aromatic ring in the H-MIM ligand can be distinguished through the band at 2929 cm^{-1}, which is a result of the C–H bond's stretching mode. The principal absorption bands of ZIF-8 can be seen in the composite structure according to the FTIR spectra of Ag. This reveals that the ZIF-8 framework is unaffected by the presence of dopant. The band of the O–H bending vibration is at 1633 cm^{-1}.[36] At 1110 cm^{-1} B–H bending vibration and 2010–2516 cm^{-1} B–H stretching was found depicting the presence of $NaBH_4$.[33]

3.4. Optical study

The photocatalytic effect of semiconducting photocatalysts was anticipated by measuring the wavelength regime of light absorbance presented in Fig. 6(a). All the composites showed a strong absorption peak in the range 300–400 nm. Compared

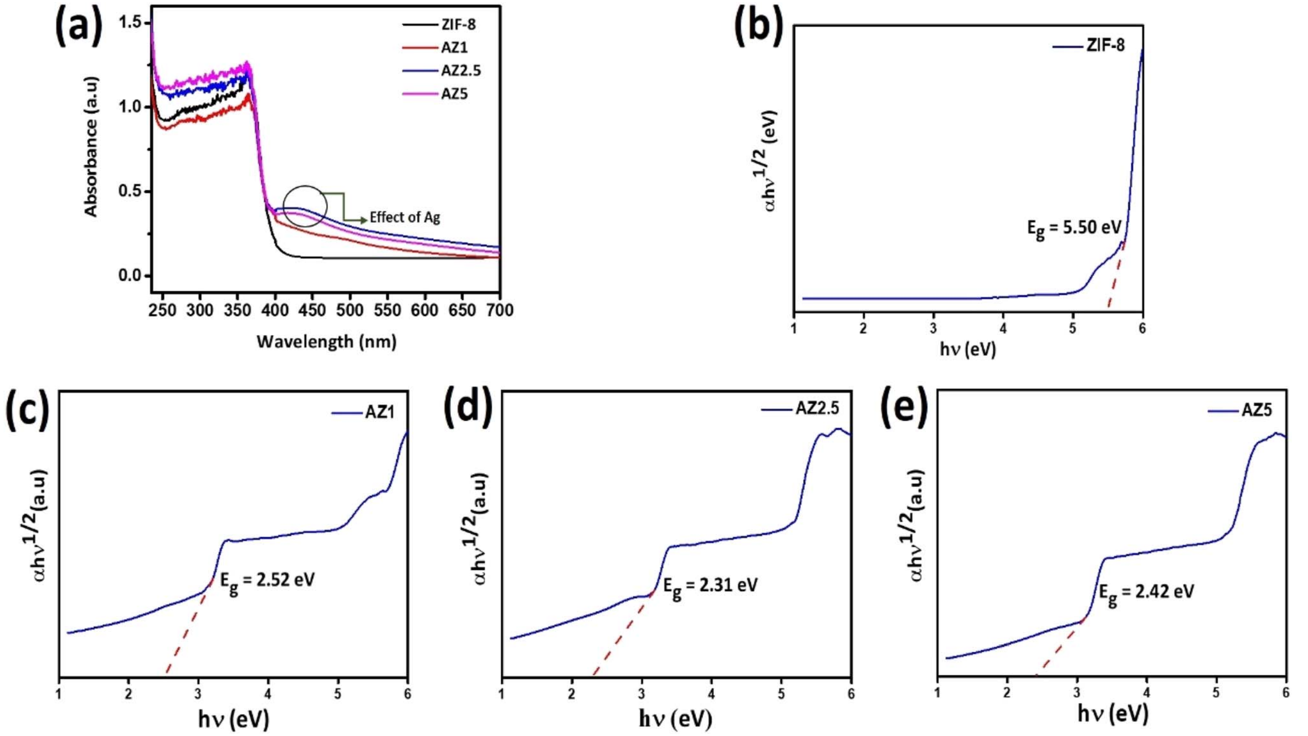

Fig. 6 (a) Diffuse reflectance spectra of all composites and (b–e) band gap energy (E_g) of ZIF-8, AZ1, AZ2.5 and AZ5.

Table 1 Calculated band-gap of the materials

Composites	Indirect bandgap (eV)
ZIF-8	5.50
AZ1	2.52
AZ2.5	2.31
AZ5	2.42

with ZIF-8 and AZ1, the AZ2.5 and AZ5 exhibited a broader and stronger absorption in the visible light region. The band was red-shifted towards visible light (400–500 nm) which can be attributed to the localized surface plasmon resonance of the silver nanoparticle and the unique heterojunction structure of Ag and ZIF-8 facilitate the transfer of charge carriers through the interface. This shows coupling of silver can enhance the light absorbance efficiently. The structure of band-gap energy plays an essential role in determining the photocatalytic activity of the sample. The band gaps of the as-prepared samples were estimated by the Kubelka–Munk plots or Tauc plot.[36,37] The following is the relationship between absorbance and incident photon energy:

$$(\alpha h\nu)^{\gamma} = \beta(h\nu - E_g)$$

The Tauc plot, which plots $(\alpha h\nu)^{\gamma}$ *versus* $h\nu$, is used to calculate the band gap. Where, α refers to the absorption coefficient, γ denotes the nature of the electronic transition, that is, when $\gamma = 2$ it is a direct allowed transition and when it is equal to 1/2, it is an indirect allowed transition. Band gap energy denoted by E_g, h and ν refer to the Plank's constant and incident light frequency respectively and β donates the proportionality constant. Herein, the band gap of pristine ZIF-8 and Ag modified ZIF-8 composites are calculated through indirect allowed transitions. The band gap energy of various samples is drawn by the linear fit curve shown in Fig. 6(b)–(e) represented in Table 1. The narrow band gap observed at the Ag nanoparticle loaded composites may be due to the formation of Schottky junction formed at the interface of Ag nanoparticle and ZIF-8 substrate. Thereby Fermi level come closer to the CB of ZIF-8 which helps in capture of photo-induced electron and leads to accumulation of electrons on Ag nanoparticle and thereby increases the photo-oxidation efficiency of CIP.

3.5. Morphological study

The microstructure, EDS spectra and elemental mapping of ZIF-8 and AZ5 was analysed and shown in Fig. 7(a)–(f). Fig. 7(a) exhibits the SEM image of ZIF-8 depicting long grain structure. Fig. 7(b) depicts elemental mapping of ZIF-8 having C, N, O, Zn as elements along with EDS spectra. Fig. 7(c) shows the histogram distribution curve of ZIF-8 having particle size with mean value of 53.44 nm and standard deviation of 18.09 nm. The agglomeration of Ag particles with ZIF-8 was found in Fig. 7(d). The elemental mapping of AZ5 having C, N, O, Zn, Ag, Na and B as elements along with EDS spectra shown in Fig. 7(e). Fig. 7(f) shows histogram distribution curve of AZ5 having particle size with mean value of 29.48 nm and standard deviation of 14.04 nm.

Distribution of Ag particles on the surface of ZIF-8 was studies through HRTEM. Ag nanoparticles were discovered to

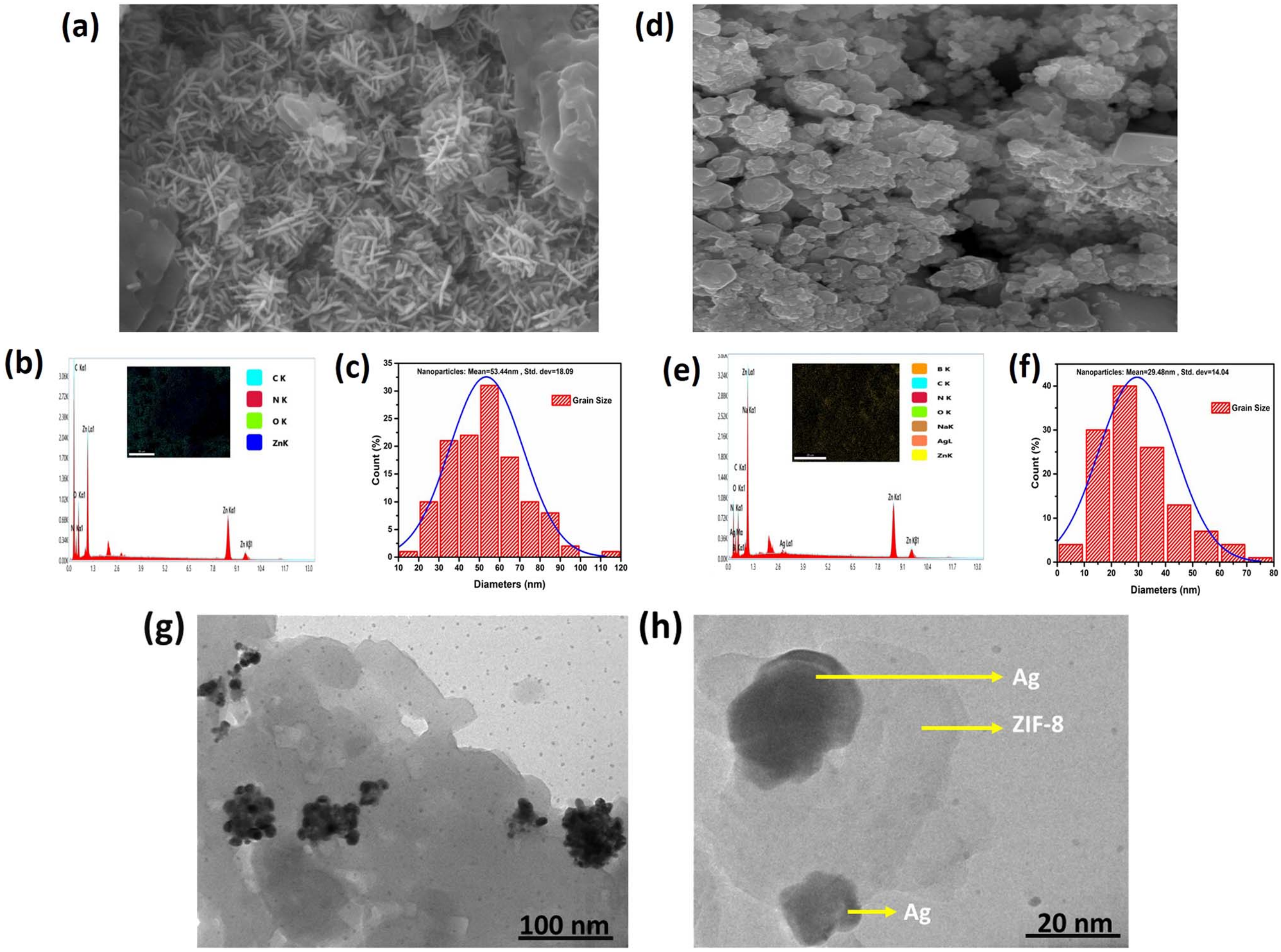

Fig. 7 (a, d) SEM micrographs (b, e) EDS spectra with elemental mapping (c, f) crystal size distribution graph of ZIF-8 and AZ5 respectively and (g, h) HRTEM images of AZ5.

be disseminated and grown on the surface of ZIF-8 to create the Ag@ZIF-8 composite, as illustrated in Fig. 7(g) and (h). Furthermore, the resulting composite demonstrated that Ag nanoparticles are encapsulated within the surface of the zeolitic imidazolate framework. The presence of Ag and ZIF-8 in the composite was confirmed by these findings.

3.6. N_2 sorption analysis

Brunauer–Emmett–Teller (BET) analysis was used to assess the N_2 sorption isotherms of ZIF-8, optimised AZ2.5 and AZ5 crystals and the findings are shown in Fig. 8. The BET surface area of ZIF-8, AZ2.5 and AZ5 were approximately obtained 36.5 m^2 g^{-1}, 17.5 m^2 g^{-1} and 0.403 m^2 g^{-1} respectively. As loading of Ag nanoparticle increases, surface area gradually decreases. However, AZ2.5 showed the better photo-oxidation of CIP than neat ZIF-8 because of synergistic effect between Ag nanoparticle and ZIF-8. The pore volume and pore diameter of ZIF-8, AZ2.5 and AZ5 were given in Table 2. From the data it is clear that pore volume and pore diameter gradually decreases as the Ag content increases. This confirms that Ag nanoparticles are well dispersed on the ZIF-8 surface. Based on IUPAC, which showed

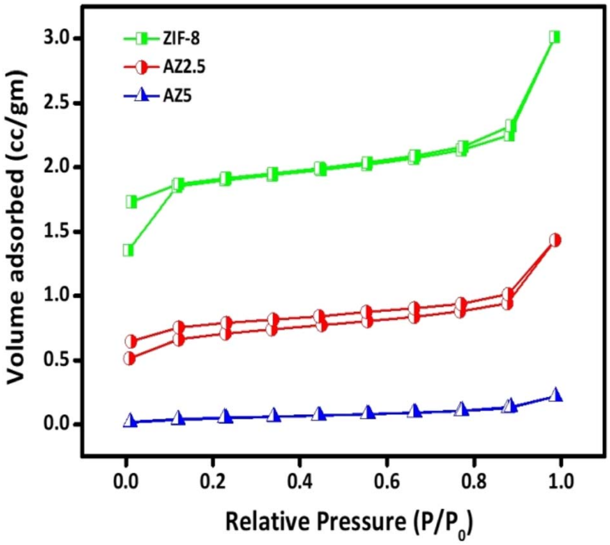

Fig. 8 Nitrogen sorption isotherms of the prepared catalysts.

Table 2 The materials' surface characteristics as synthesized

S. no.	Name of the catalyst	Surface area ($m^2\ g^{-1}$)	Pore volume ($cm^3\ g^{-1}$)	Pore diameter (nm)
1	ZIF-8	36.5139	8.019	4.106
2	AZ2.5	17.4417	2.655	4.086
3	AZ5	0.403	1.628	4.085

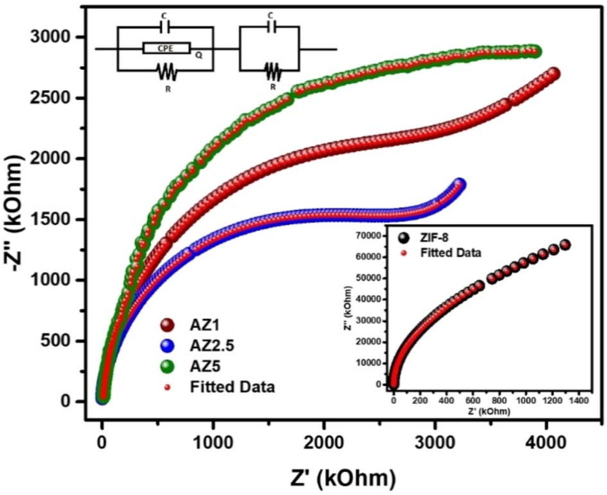

Fig. 9 Nyquist Plot for ZIF-8, AZ1, AZ2.5 and AZ5.

Table 3 MIC of samples against *S. aureus* and *E. coli*

Name of the sample	MIC ($\mu g\ mL^{-1}$) *S. aureus*	MIC ($\mu g\ mL^{-1}$) *E. coli*
ZIF-8	300	1200
AZ1	150	300
AZ2.5	37.5	75
AZ5	9.37	37.5

the microstructure of the MOFs, all samples' adsorption behaviour can be categorised into type 1 curve.

3.7. EIS analysis

The electrical response of pristine ZIF-8, AZ1, AZ2.5 and AZ5 were examined using an LCR metre of type No-N4L PSM, 1735 all over a wide frequency range (1 kHz to 1 MHz). The Nyquist plot analysis offers a precise information regarding the effect of electron–hole separation in these samples. The plot could demonstrate how grain and grain boundaries affect the electrical conduction process. The electrical impedance spectra were calculated from the Nyquist plot using the ZSIMPWIN version 2.0 software code. The computed data and the experimental data were identical after modelling the Nyquist plot curves with an analogous circuit {(CQR)(CR)}. Fig. 9 shows that the Nyquist plot for the AZ2.5 catalyst has a decreasing radius of semi-circular character than other materials. The radius of the semicircle shows the rate of photocatalytic reaction on the photocatalyst surface. A decrease in semicircle radius indicates drop in solid-state interface layer resistance, which leads to an increase in electron–hole pair transfer rate. As a result, electron aggregation increased, lowering the recombination rate. However, the lowered semi-circle radius of the AZ2.5 composite exhibits the lowest resistance, which is consistent with the material's photocatalytic activity.

3.8. Antibacterial ability evaluation

3.8.1. Minimum inhibitory concentration (MIC). A MIC ($\mu g\ mL^{-1}$ Minimum Inhibitory Concentration) is described as the lowest concentration of an antimicrobial agent, when used in specific circumstances, inhibits a microbe from growing visibly. The antibacterial activities against Gram negative (*E. coli*) and Gram positive (*S. aureus*) were assessed by MIC followed by broth microdilution method through 96 well plate. Initially dimethyl sulfoxide solutions of ZIF-8, AZ1, AZ2.5 and AZ5 ($10\ mg\ mL^{-1}$) was taken and were experimented. Optical density (OD) was measured at 600 nm on a microplate reader. The

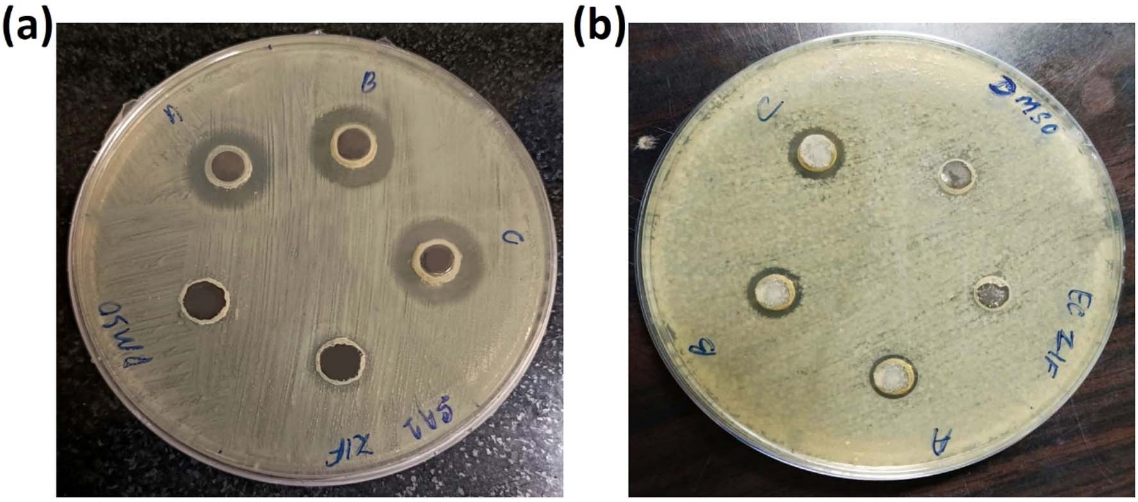

Fig. 10 Inhibition zone of (a) *S. aureus* and (b) *E. coli* with DMSO, ZIF-8, (A) AZ1, (B) AZ2.5 and (C) AZ5 respectively.

overall result was discussed in Table 3. Based on the MIC test, it could be concluded that AZ5 9.37 μg mL^{-1}, 37.5 μg mL^{-1} for *S. aureus* and *E. coli* respectively found to serve as a broad-spectrum antibacterial agent as compared to AZ1, AZ2.5 and ZIF-8. The antibacterial process has previously been attributed to the fact that dissolved O_2 can gradually oxidise Ag nanoparticles into Ag^+. The discharged Ag^+ could cause cytomembrane disruption, resulting in intracellular content leakage and bacterial demise.[38–41]

3.8.2. **Inhibition zone test.** To compare the antibacterial activity of ZIF-8, AZ1, AZ2.5 and AZ5, the inhibition zone was evaluated on agar plates. As indicated in Fig. 10(a) and (b), AZ5 performed better against *S. aureus* and *E. coli*. No zone of inhibition zone was found for pure ZIF-8 in *S. aureus* and *E. coli* respectively. Whereas the diameter of values for AZ1 were 15 mm and 10 mm for *S. aureus* and *E. coli*, respectively, the inhibition zone diameter values for AZ2.5 were 17 mm and 11 mm for *S. aureus* and *E. coli* respectively and the inhibition zone diameter of AZ5 was around 18 mm and 13 mm for *S. aureus* and *E. coli* respectively. This represents that more the value of Ag, killing activity was increased in both *S. aureus* and *E. coli* than rest of the material.

3.8.3. **Morphology of bacteria.** Bacterial morphology found to be fine in case of control in both the strains of bacteria including *E. coli* and *S. aureus* shown in Fig. 11(a) and (c) whereas after treatment by the optimized sample composite AZ5 the morphology of the bacteria was found to be completely destroyed by showing shrinkage and bursting of the cells with release of cellular components in both the cases *E. coli* and *S. aureus* respectively seen in Fig. 11(b) and (d).

3.8.4. **Photocatalytic disinfection mechanism.** By serving as a bioactive substance with a bioactive metal, linker or both, MOFs can be used to fight bacterial infections. They can also serve as a platform for the transport and release of antibacterial medications. Fig. 12 demonstrates how created antibacterial composites were evaluated using the agar well diffusion method against Gram-negative *E. coli* and Gram-positive *S. aureus* bacterial strains to determine the inhibition zone width. In terms of antibacterial efficacy against both Gram-negative and Gram-positive bacteria, the AZ5 combination beat pure ZIF-8. It was discovered that the mean inhibition zone of AZ5 was greater than that of pure ZIF-8. The cellular membranes' surface is covered in silver particles from AZ5, which clump together and interfere with energy-related functions including respiration and permeability. In

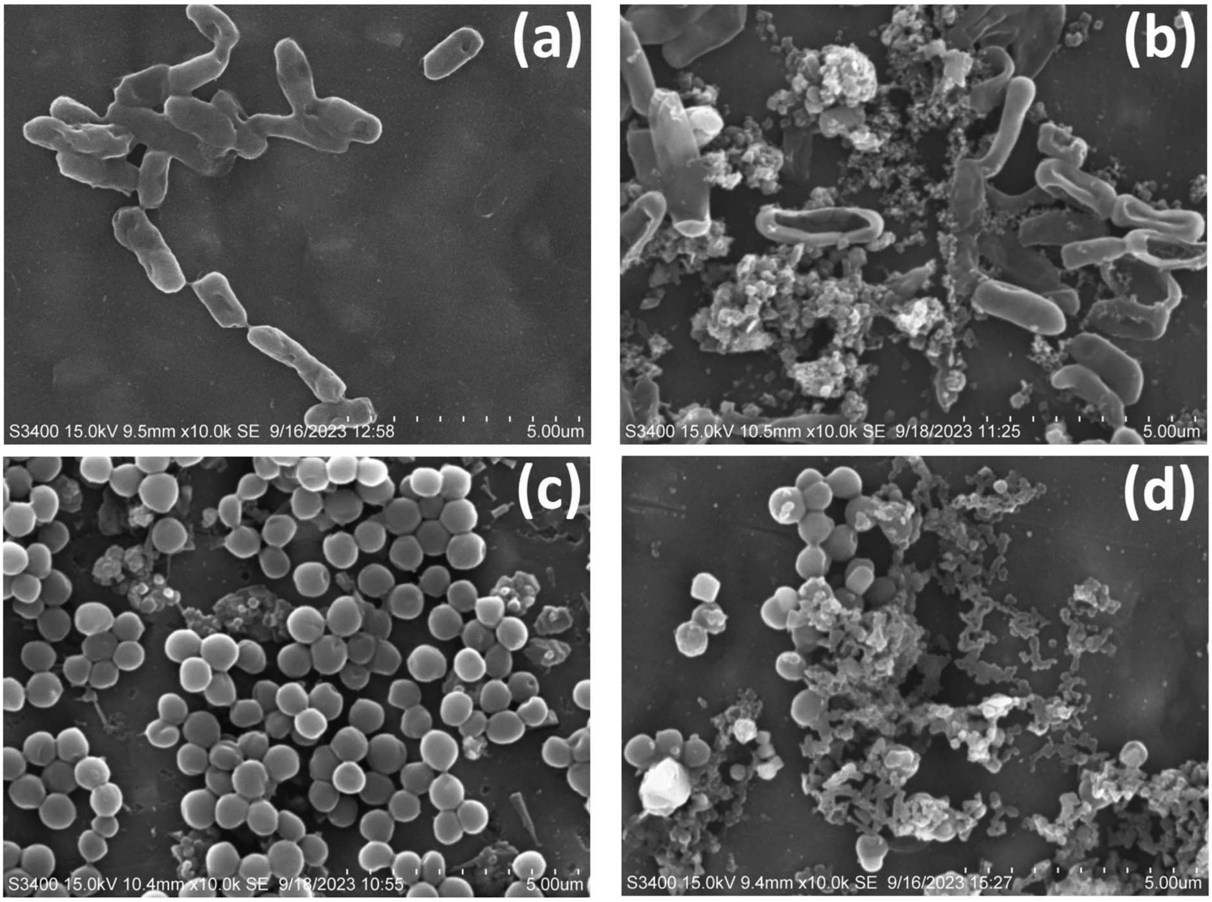

Fig. 11 SEM images of antibacterial activity (a) *E. coli* control, (b) *E. coli* after treatment with AZ5, (c) *S. aureus* and (d) *S. aureus* after treatment with AZ5.

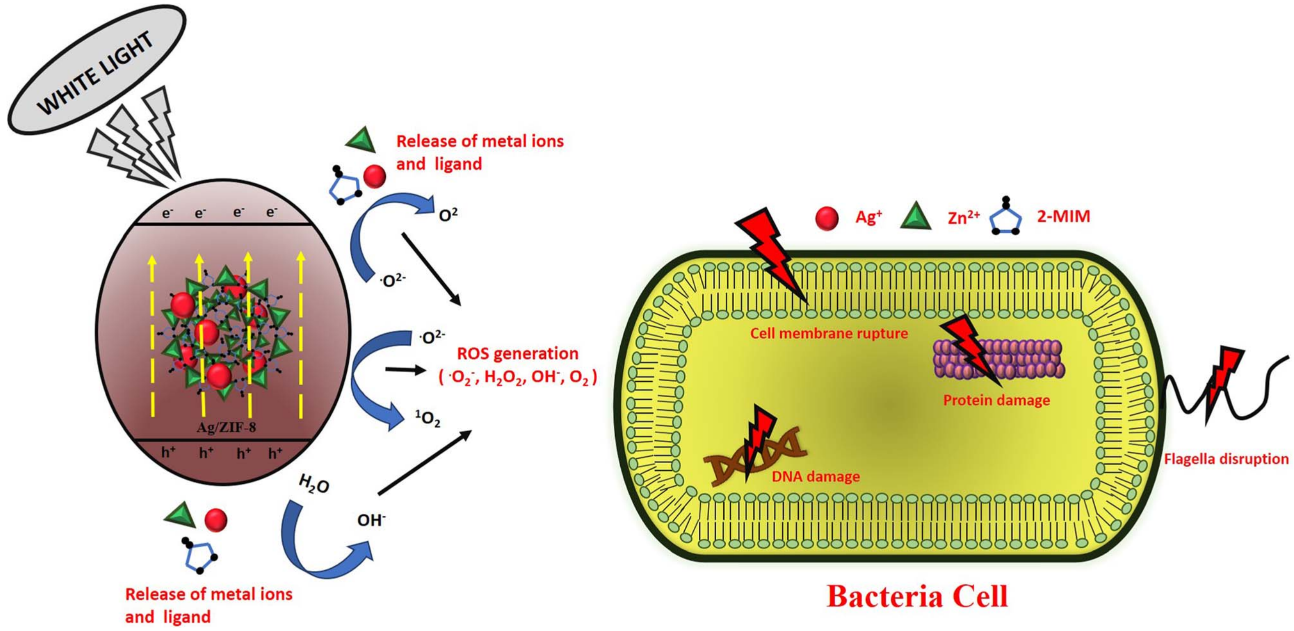

Fig. 12 Schematic representation of antibacterial mechanism.

Table 4 Displays a previous study on antibacterial activity using Ag/ZIF-8 composite

S. no.	Sample	Bacterial strain	Method used	References
1	AgNps@ZIF-8	*E. coli* and *S. aureus*	Growth inhibition of bacteria (GIS) and colony forming units	31
2	Ag@ZIF-8	*E. coli* and *S. aureus*	Inhibitory zone	36
3	Ag@ZIF-8	*E. coli* and *B. subtilis*	Minimum inhibitory concentration and inhibitory growth in LB plate	43
4	AZ5	*E. coli* and *S. aureus*	Inhibitory zone and minimum inhibitory concentration	**Present Study**

comparison to all prior papers, the mechanism of the AZ5 composite's improved antibacterial action is summarised in Table 4 as a bioactive material. For antibacterial actions, the bacterial membrane's sulfhydryl groups could coordinate with the Ag metal centres dispersed on the ZIF-8, resulting in intimate contact between the membrane and the material. It has previously been claimed that the discharge of Ag^+ and Zn^{2+} could cause the creation of reactive oxidative species (ROS) such as superoxide anions and hydroxyl radicals, which could rupture the cell membrane and cause the leakage of cell contents.[42] Furthermore, ROS with a high oxidation potential can damage DNA and RNA, sabotaging protein expression and leading to cell apoptosis. When the photocatalyst's surface (AZ5) gets exposed to white light, an electron jumps from the VB to the CB of AZ5, whereas holes generated in the VB. In the meantime, the surrounding O_2 interacts with the electrons to produce $O^{2-\bullet}$ H_2O combines with this h^+ to produce hydroxyl ($OH^\bullet$) radical and the surrounding O_2 combines with the electrons to form $O_2^{-\bullet}$. This production of ROS is able to destroy the bacterial cell components (cell wall, membrane, proteins, DNA, RNA, ribosomes and so on) with subsequent break down of membrane and finally cell death, as indicated in the Fig. 12. The comprehensive formation process by the reactive oxygen species (ROS) is as follows:

$$\text{Ag/ZIF-8} + h\nu \rightarrow \text{Ag/ZIF-8}\ (e^- + h^+)$$

$$\text{Ag/ZIF-8} + e^- \rightarrow \text{Ag/ZIF-8}\ (e_{cb}{}^-) + Ag^+$$

$$O_2 + e_{cb}{}^- \rightarrow O_2{}^{-\bullet}$$

$$4H^+ + 2H_2O \rightarrow O_2 + 8H^+$$

$$H^+ + O_2{}^{-\bullet} \rightarrow HO_2{}^\bullet$$

$$2HO_2{}^\bullet \rightarrow H_2O_2 + O^{2-\bullet}$$

$$H_2O_2 + O_2{}^{-\bullet} \rightarrow OH^\bullet + OH^- + O_2$$

$$h^+ + OH^- \rightarrow OH^\bullet$$

3.8.5. **Haemolysis.** Haemolysis test as done to observe the biocompatibility of materials for bio-medical application. The blood agar Petri plate showed no ring of lyses against all the 4 samples ZIF-8, AZ1, AZ2.5 and AZ5 shown in Fig. 13(a). Further the optimised AZ5 was tested with 4 different increased concentration of sample (10 mg mL^{-1}, 15 mg mL^{-1}, 20 mg mL^{-1}, 25 mg mL^{-1} and 30 mg mL^{-1}) was resulted in no ring of lyses describing a positive response towards no bad impact on blood shown in Fig. 13(b).

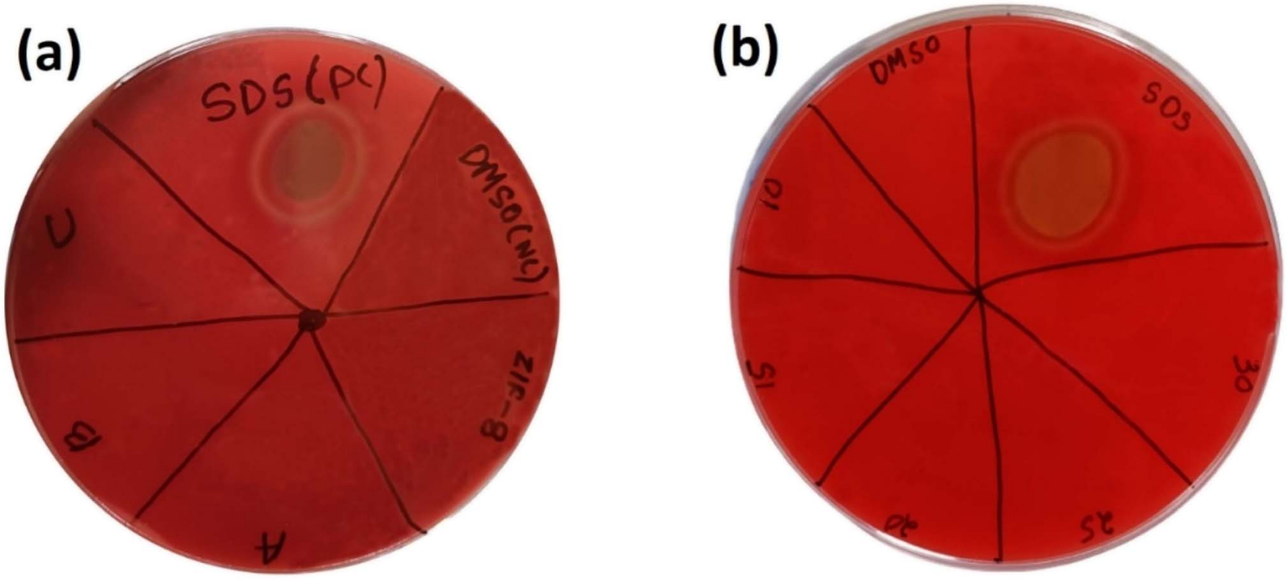

Fig. 13 Haemolytic activity in blood agar plate (a) ZIF-8, (A) AZ1, (B) AZ2.5 and (C) AZ5 with positive control (SDS) and negative control (DMSO) and (b)- varied 5 concentrations of AZ5 (optimised).

4. Photo-catalytic activity

4.1. Evaluation of photo-catalyst performance towards photo-oxidation of antibiotics under visible light

Photocatalytic application was carried out against the antibiotic drug CIP by adding 0.02 g synthesized catalysts ZIF-8, AZ1, AZ2.5 and AZ5 under sunlight. To reach the adsorption–desorption equilibrium between CIP and catalyst the reaction was carried out for 15 minutes in dark condition and then the solutions are subjected to expose under sunlight for photocatalytic degradation of CIP. The catalyst AZ2.5 was optimized and absorption spectrum was calculated within the wavelength range 200–350 nm with a 15 minutes interval of time (15, 30,45,60,75 and 90 minutes). The intensity of peak adsorption observed at 275 nm, with increase in time the adsorption peak intensity gradually decreased shown in Fig. 14(a). At 90 minutes almost all the antibiotic are absorbed on the surface of the composite and the optimum time set for photocatalytic degradation of CIP fixed to 90 minutes. Photocatalytic reactions are pH dependent and to fix the optimum pH, the adsorption process is carried out at different pH (3, 5, 7 and 9) conditions are shown in Fig. 14(b). Many authors reported that the photocatalytic degradation of CIP enhanced with rising the pH and reaching the maximum at pH ≥ 7, which is mainly related to pK_a value of CIP (pK_a = 6.01–8.74). It indicates neutral form is more sensitive to photocatalytic reaction. At acidic pH, the –COOH group present in CIP is not ionized and nitrogenous bases are fully protonated and CIP behaves more stable. When, pH ≥ pK_a (8.74) CIP molecule is negatively charged because of de-protonation of –COOH group. Hence, at neutral pH, the surface of CIP is both positively and negatively charged and behaves like a zwitterion and shown a significant increase in photocatalytic degradation of CIP. In addition to this, surface charge plays an important role in the adsorption of CIP molecule on the surface of photocatalyst. Point zero charge (Pzc) value of AZ2.5 is 8.9. When pH ≤ Pzc value, surface is positively charged and there is a better force of attraction between the catalyst and substrate and thereby increases the adsorption of CIP onto the surface of catalyst and increases the degradation efficiency. In order to know the better adsorption zeta potential of all the catalyst was calculated and shown in ESI1.† After that all the samples are directed towards sunlight for further degradation for 90 minutes at pH7. Photocatalytic degradation percentage of CIP was evaluated in the increasing order such as: AZ2.5 (82.3) > AZ5 (75.6) > AZ1 (73.6) > pure ZIF-8 (61) shown in Fig. 14(c) with an error calculation shown in ESI2.† Again, to prove the photocatalytic behaviour different operational parameters are responsible to inhibit the rate of the reaction. Different amount of catalyst (0.02 g, 0.04 g, 0.06 g, 0.08 g, and 1 g) was added to the reaction medium. The result obtained that the degradation rate increased and attain 82.3% at 90 minutes time by increasing the catalyst dose from 0.02 g to 0.06 g and after that it remain constant shown in Fig. 14(d). The excess amount of catalyst may block the light irradiation and may restrict the photocatalytic oxidation rate of CIP. Therefore, the optimum dose of catalyst was set to 0.04 g. The rate of photocatalytic degradation of CIP with respect to time was followed the pseudofirst order reaction kinetics. Fig. 14(e) the kinetic studies represent the impact of CIP on photocatalytic degradation at different concentrations of CIP (20, 40, 60 and 80 ppm) at different time interval (15, 30, 45, 60, 75 and 90 minutes). The experimental data was successfully matched to the 1st order kinetics equation:

$$K_{\text{app}}t \times 2.303 = \log C_0/C_t$$

$$K_{\text{app}} = \log C_0/C_t \times 2.303/t$$

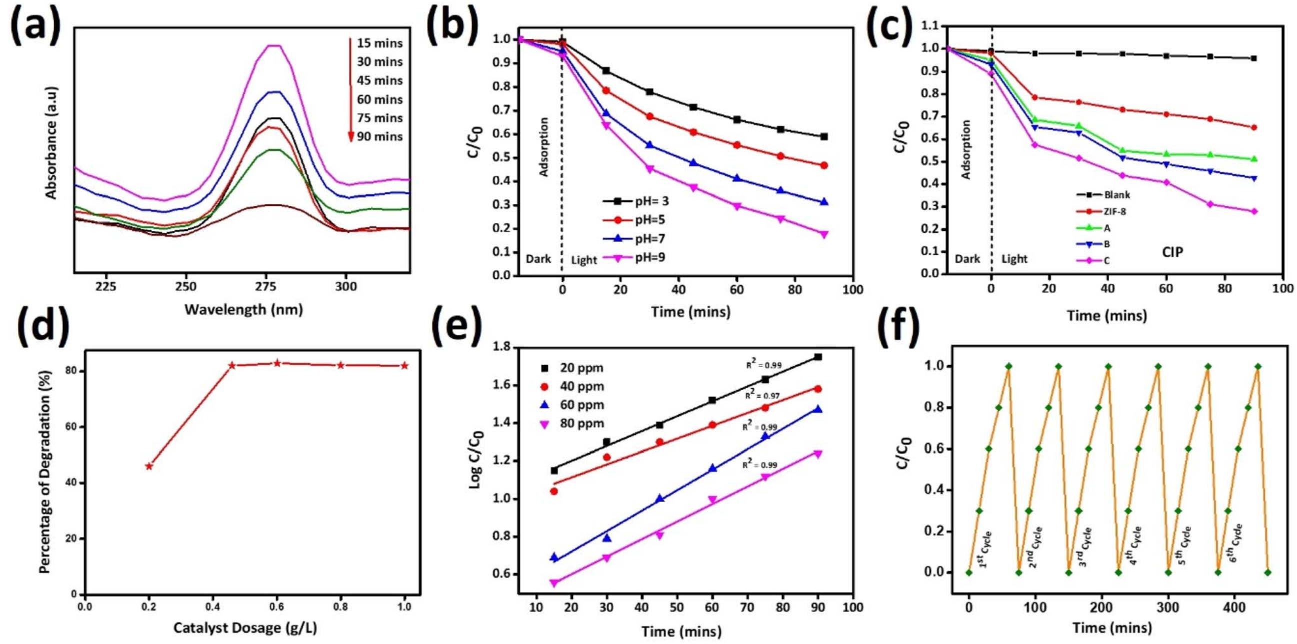

Fig. 14 (a) Photo-degradation of CIP by AZ2.5 at various intervals of time (b) effect of pH (c) CIP photo-degradation by various catalysts over varied time periods (d) effect of dosage of catalyst on degradation of CIP (e) pseudo-1st order reaction kinetics in different concentrations and (f) Reusability test of AZ2.5.

Fig. 14(e) illustrates the relationship between C_t (the final concentration of CIP solution after illumination time t) and C_0 (the initial concentration of CIP solution) as C_0/C_t a function of deterioration time. K_{app} is the rate constant of a pseudo-first order kinetics. According to the degradation efficiency, AZ2.5 has the highest degradation rate constant (K_{app}) shown in Table 5. The stability and recyclability of photocatalysts plays a crucial role for practical application as shown in Fig. 14(f). Our optimized sample AZ2.5 after 6 consecutive runs, showed that there is no decrease in the photo-reduction capacity of the material depicting the Ag and other material like Zn are not leached to the solution, which proves it has a greater stability and sustainability. So, Ag/ZIF-8 is an excellent photocatalyst for the degradation of antibiotic drug pollution in waste water.

4.2. Photocatalytic mechanism

It is well-known that, the active species play an important role in photocatalytic degradation process. To know the active species responsible for the reaction mechanism of CIP, trapping experiment was carried out in Fig. 15. The photocatalyst chosen for experiment was AZ2.5. To trap the potential active radicals $O_2^{-\bullet}$, $OH^{\bullet}$, h^+ and e^- several trapping agents like *para*-benzoquinone, iso-propanol, citric acid and DMSO respectively are utilised. The concentration of scavengers is maintained 1 mM and the reaction condition is maintained same throughout the reaction. The result revels that the degradation efficiency decreased by the addition of PBQ and IPA, while there is no significant change is observed by the addition of DMSO. However, the addition of citric acid also declines the efficiency of CIP degradation. From the above result, it is seen that the oxidative species *i.e.*, $OH^{\bullet}$, $O_2^{-\bullet}$, and h^+ are accountable for the degradation of CIP. Few previous reports are cited in comparison to present study was represented in Table 6.

Table 5 Kinetic information obtained from the produced CIP sample

Concentration of CIP (ppm)	K_{app} (min^{-1})	Regression coefficient (R^2)
20	0.0174	0.99
40	0.0197	0.98
60	0.0214	0.99
80	0.0240	0.98

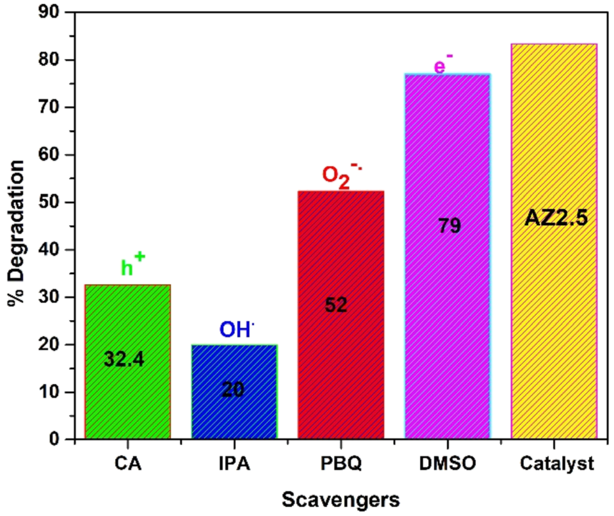

Fig. 15 Scavenging test of 40 mgL^{-1} CIP taking AZ2.5 as catalyst.

Table 6 Displays an earlier research study on reduction of Ag/ZIF-8 composite

S. no.	Catalyst	Degrading element	Concentration of degradation element	Light source	Degradation percentage and time	References
1	AgNPs@ZIF-8s/P-OCBs	Rhodamine B, Methylene blue	150 mg L^{-1}	Visible	100%, 10 min	31
2	AgNPs@ZIF-8	Methylene blue and Congo red	10 mg/20 mL	Visible, UV light	97%, 100%, 120 min, 60 min	44
3	Ag@ZIF-8	Methyl orange, Rhodamine B	80 mg L^{-1}	UV light	100%, 93%, 30 min	36
4	AZ5	CIP	40 mg L^{-1}	UV light	82.3%, 75 min	Present study

Scheme 1 shows the best possible mechanistic pathway of photocatalytic degradation of CIP, over Ag loaded ZIF-8 under the illumination of solar light. Modification of ZIF-8 by Ag creates the defect/oxygen vacancies (V_O) and Zn$^+$ cites in ZIF-8 MOF crystal. With loading of Ag, electrons transferred from Ag(0) to Zn^{2+} and reduced to Zn$^+$ and Ag$^+$ ions are formed. The generated vacancies favour the formation of some defect energy level below the conduction band of ZIF-8 due to Ag 4d states inserted within the band gap of ZIF-8 and helps in the reduction of the band gap of the composite and electrons are excited from the valence band to conduction band of ZIF-8 band holes are created on the valence band. These photo-generated electron and hole pair moving on the surface of composite. Another interpretation for the second mode is work function perspective of Ag nanoparticle and the substrate where it is deposited. Because of dissimilar work functions between Ag nanoparticle (ϕ = 4.25 eV) and ZIF-8 (ϕ = 5.7 eV) formed a Schottky barrier at the interface when both sides are come closer. Mostly hot plasmonic electrons migrate from the lower work function (Ag nanoparticle) to higher work function (ZIF-8) until attaining the equilibrium between two Fermi level. Under solar light illumination, due to high LSPR enables the generation of strong electron density and enriched on the surface of Ag nanoparticle which can raise itself Fermi level and facilitate the electrons injected into the conduction band of ZIF-8. The photo-induced surface holes react with surface hydroxyl groups (OH$^-$) of the composite (Ag/ZIF-8) and produce OH$^\bullet$ radical and the electrons react with surface adsorbed O_2 forming $O_2^{-\bullet}$ radical. At the same time, Ag$^+$ (Ag^0 + e$^-$ → Ag$^+$) react with the photo generated holes (h$^+$) and Ag^{2+} is formed. This *in situ* generated Ag^{2+} again oxidised the OH$^-$ group to produce OH$^\bullet$ radical. The electrons are further trapped by Ag$^+$ and reduced to Ag(0) and the released electron react with O_2 to form $O_2^{-\bullet}$ and helps in electron–hole channelization and reduced the recombination rate. Again, the electron present in ZIF-8 reacts with surface adsorbed O_2 to form $O_2^{-\bullet}$ and further react with surface adsorbed H_2O to form OH$^\bullet$. Hence, OH$^\bullet$ is the most reactive oxidative powerful species to depollute the antibiotics. The detailed mechanism is explained below.

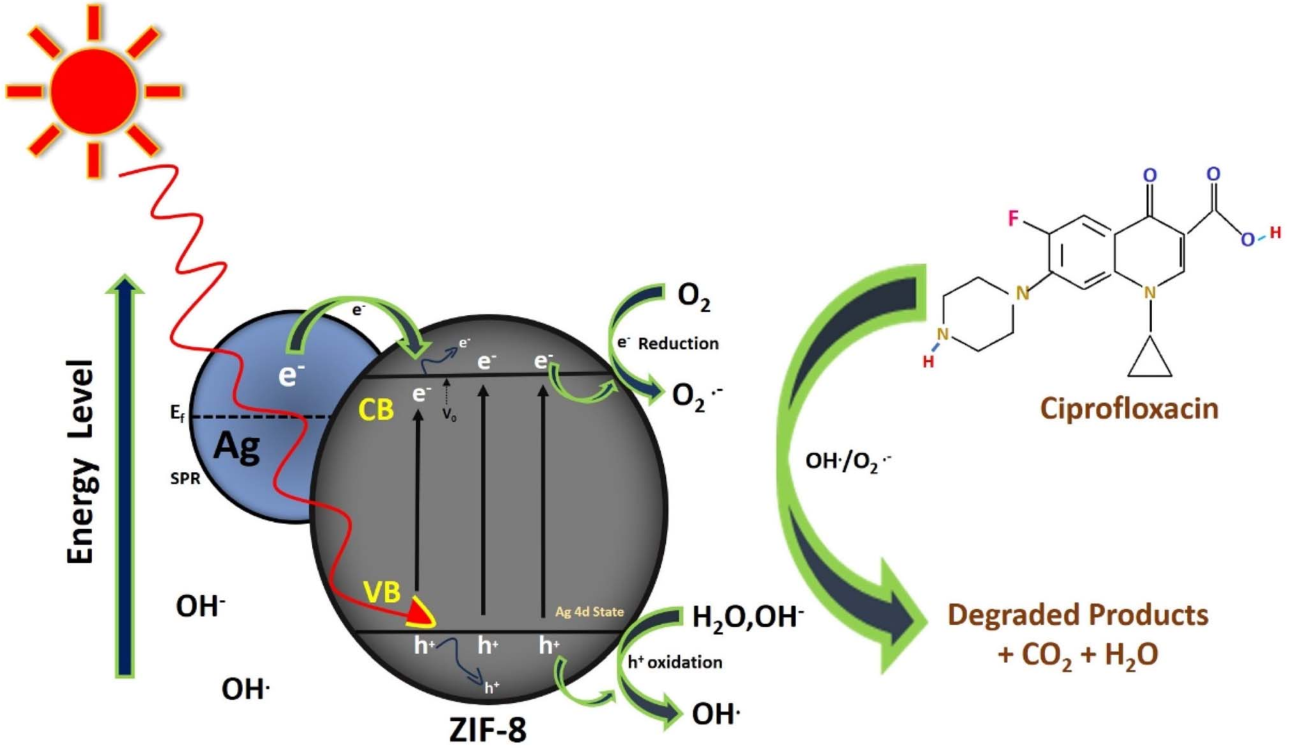

Scheme 1 Photocatalytic mechanism of CIP drug.

$$\mathrm{Ag/ZIF\text{-}8} + h\nu \rightarrow \mathrm{Ag/ZIF\text{-}8(e_{cb}^{-})} + \mathrm{Ag/ZIF\text{-}8(h_{vb}^{+})}$$

$$\mathrm{H^{+} + OH^{-} \rightarrow OH^{\bullet}}$$

$$\mathrm{O_2 + e^{-} \rightarrow O_2^{-\bullet}}$$

$$\mathrm{Ag^{0} + e^{-} \rightarrow Ag^{+} + O_2^{-}}$$

$$\mathrm{Ag^{+} + h^{+} \rightarrow Ag^{2+}}$$

$$\mathrm{Ag^{2+} + OH^{-} \rightarrow OH^{\bullet} + Ag^{+}}$$

$$\mathrm{Ag^{+} + e^{-} \rightarrow Ag^{0}}$$

$$\mathrm{Ag^{0} + Zn^{2+} \rightarrow Zn^{+} + Ag^{+}}$$

$$\mathrm{Zn^{+} + O_2 \rightarrow Zn^{2+} + O_2^{-}}$$

$$\mathrm{O_2^{-} + h^{+} \rightarrow O^{-}}$$

$$\mathrm{O^{-} + adsorbed\ H_2O \rightarrow OH^{-} + OH^{\bullet}}$$

$$\mathrm{CIP + OH^{\bullet} \rightarrow H_2O + CO_2 + degraded\ products.}$$

5. Conclusions

(1) Using the sol–gel process, plasmonic Ag/ZIF-8 composite was fashioned by adding Ag at various molar concentrations (1 mM, 2.5 mM and 5 mm) to ZIF-8.

(2) The optimized AZ2.5 founds to be best by showing highest photocatalytic efficiency towards the drug CIP *i.e.*, 82.3% due to adsorption in the spectrum of visible light increases by the loading of Ag nanoparticle.

(3) The narrow band gap observed at the Ag nanoparticle loaded composites may be due to the formation of Schottky junction formed at the interface of Ag nanoparticle and ZIF-8 substrate helps in efficient electron–hole channelization.

(4) Due to LSPR (Localised Surface Plasmon Resonance) as well as the efficient movement and separation of the interfaces of photo-generated charge carriers in Ag2.5/ZIF-8 may be the causes of this increase in photocatalytic degradation.

(5) Even after, six cycles of the reusability test, there was no discernible leaching proves the stability and sustainability of the composite.

(6) The loading of Ag in AZ5 was optimized for playing major role in antibacterial activity by generating reactive oxygen species (ROS) and synergistic with $\mathrm{Zn^{2+}}$ ion in ZIF-8.

(7) This suggests that the photocatalyst remains stable, environmentally safe with no toxicity to blood can be utilized for environmental remediation and alternatives to drug resistance bacteria.

Conflicts of interest

There are no conflicts to declare.

References

1 J. Acar and B. Rostel, *Rev. Sci. Tech. Off. Int. Epizoot.*, 2001, **20**, 797–810.

2 L. Yan, A. Gopal, S. Kashif, P. Hazelton, M. Lan, W. Zhang and X. Chen, *Chem. Eng. J.*, 2022, **435**, 134975.

3 G. Wyszogrodzka, B. Marszałek, B. Gil and P. Dorożyński, *Drug Discov. Today*, 2016, **21**, 1009–1018.

4 Y. Ben, C. Fu, M. Hu, L. Liu, M. H. Wong and C. Zheng, *Environ. Res.*, 2019, **169**, 483–493.

5 M. Yousefi, M. Dadashpour, M. Hejazi, M. Hasanzadeh, B. Behnam, M. de la Guardia, N. Shadjou and A. Mokhtarzadeh, *Mater. Sci. Eng. C*, 2017, **74**, 568–581.

6 M. Singh, S. Singh, S. Prasad and I. S. Gambhir, *Dig. J. Nanomater. Biostruct.*, 2008, **3**, 115–122.

7 P. F. McDermott, S. M. Bodeis, L. L. English, D. G. White, R. D. Walker, S. Zhao, S. Simjee and D. D. Wagner, *J. Infect. Dis.*, 2002, **185**, 837–840.

8 T. Thai, B. H. Salisbury and P. M. Zito, in *StatPearls*, StatPearls Publishing, 2023.

9 M. Esfahanian, M. A. Ghasemzadeh and S. M. H. Razavian, *Artif. Cells Nanomed. Biotechnol.*, 2019, **47**, 2024–2030.

10 D. Kanakaraju, B. D. Glass and M. Oelgemöller, *J. Environ. Manage.*, 2018, **219**, 189–207.

11 P. V. Nidheesh, C. Couras, A. V Karim and H. Nadais, *Chem. Eng. Commun.*, 2022, **209**, 390–432.

12 T. Ma, C. Yang, L. Guo, R. A. Soomro, D. Wang, B. Xu and F. Fu, *Appl. Catal. B Environ.*, 2023, **330**, 122643.

13 L. Xie, Z. Yang, W. Xiong, Y. Zhou, J. Cao, Y. Peng, X. Li, C. Zhou, R. Xu and Y. Zhang, *Appl. Surf. Sci.*, 2019, **465**, 103–115.

14 X. Dong, Y. Li, D. Li, D. Liao, T. Qin, O. Prakash, A. Kumar and J. Liu, *CrystEngComm*, 2022, **24**, 6933–6943.

15 T. Xia, Y. Lin, W. Li and M. Ju, *Chin. Chem. Lett.*, 2021, **32**, 2975–2984.

16 X. Zhang, F. Peng and D. Wang, *J. Funct. Biomater.*, 2022, **13**, 215.

17 M. Shen, F. Forghani, X. Kong, D. Liu, X. Ye, S. Chen and T. Ding, *Compr. Rev. Food Sci. Food Saf.*, 2020, **19**, 1397–1419.

18 T. R. Cook, Y.-R. Zheng and P. J. Stang, *Chem. Rev.*, 2013, **113**, 734–777.

19 X. Hou, J. Wang, B. Mousavi, N. Klomkliang and S. Chaemchuen, *Dalton Trans.*, 2022, **51**, 8133–8159.

20 T. Rasheed, K. Rizwan, M. Bilal and H. M. N. Iqbal, *Molecules*, 2020, **25**, 1598.

21 Y. Shan, G. Zhang, Y. Shi and H. Pang, *Cell Reports Phys. Sci.*, 2023, **4**(3), 101301.

22 J. A. Thompson, C. R. Blad, N. A. Brunelli, M. E. Lydon, R. P. Lively, C. W. Jones and S. Nair, *Chem. Mater.*, 2012, **24**, 1930–1936.

23 L. du Bourg, A. U. Ortiz, A. Boutin and F.-X. Coudert, *APL Mater.*, 2014, **2**, 124110.

24 H. Fei, J. F. Cahill, K. A. Prather and S. M. Cohen, *Inorg. Chem.*, 2013, **52**, 4011–4016.

25 Z. Mo, D. Tai, H. Zhang and A. Shahab, *Chem. Eng. J.*, 2022, **443**, 136320.

26 D. Zou, D. Liu and J. Zhang, *Energy Environ. Mater.*, 2018, **1**, 209–220.
27 Y. Deng, Y. Wu, G. Chen, X. Zheng, M. Dai and C. Peng, *Chem. Eng. J.*, 2021, **405**, 127004.
28 Y. Yu, Z. Zhou, G. Huang, H. Cheng, L. Han, S. Zhao, Y. Chen and F. Meng, *Water Res.*, 2022, 118901.
29 J. Li, Z. Lou and B. Li, *Chin. Chem. Lett.*, 2022, **33**, 1154–1168.
30 L. Panda, A. Pradhan, B. Nanda, *et al.*, *Inorg. Chem. Commun.*, 2023, **150**, 110486.
31 X. Meng, C. Duan, Y. Zhang, W. Lu, W. Wang and Y. Ni, *Compos. Sci. Technol.*, 2020, **200**, 108384.
32 X. Yang, H. Chai, L. Guo, Y. Jiang, L. Xu, W. Huang, Y. Shen, L. Yu, Y. Liu and J. Liu, *Colloids Surf. B Biointerfaces*, 2021, **205**, 111920.
33 D. Rohendi, N. Syarif and E. K. Wati, *IOP Conf. Ser. Earth Environ. Sci.*, 2019, **248**, 12008.
34 S. Feng, X. Jia, J. Yang, Y. Li, S. Wang and H. Song, *J. Mater. Sci. Mater. Electron.*, 2020, **31**, 22534–22545.
35 R. Nayak, F. A. Ali, P. G. R. Achary and B. Nanda, *Inorg. Chem. Commun.*, 2023, **147**, 110206.
36 J. Abdi, *Colloids Surf. A Physicochem. Eng. Asp.*, 2020, **604**, 125330.
37 N. Chang, Y.-R. Chen, F. Xie, Y.-P. Liu and H.-T. Wang, *Colloids Surf. A Physicochem. Eng. Asp.*, 2021, **616**, 126351.
38 S. Koppala, Y. Xia, L. Zhang, J. Peng, Z. Chen and L. Xu, *Ceram. Int.*, 2019, **45**, 15116–15121.
39 Q. Jiang, Z. Lin, B. Gu, C. Pang and X. Wang, *Ind. Crops Prod.*, 2020, **158**, 112987.
40 Z.-K. Tan, J.-L. Gong, S.-Y. Fang, J. Li, W.-C. Cao and Z.-P. Chen, *Appl. Surf. Sci.*, 2022, **590**, 153059.
41 F. Mo, H. Li, Y. Li, W. Cui, M. Wang, Z. Li, R. Chai and H. Wang, *Ecotoxicol. Environ. Saf.*, 2020, **195**, 110499.
42 J. Cui, D. Wu, Z. Li, G. Zhao, J. Wang, L. Wang and B. Niu, *Ceram. Int.*, 2021, **47**, 15759–15770.
43 Y.-F. Guo, W.-J. Fang, J.-R. Fu, Y. Wu, J. Zheng, G.-Q. Gao, C. Chen, R.-W. Yan, S.-G. Huang and C.-C. Wang, *Appl. Surf. Sci.*, 2018, **435**, 149–155.
44 G. Fan, X. Zheng, J. Luo, H. Peng, H. Lin, M. Bao, L. Hong and J. Zhou, *Chem. Eng. J.*, 2018, **351**, 782–790.